



# New insights into the effects of surface nanocrystallization on the oxidation of 321 austenitic stainless steel in a humid oxygen environment at 1000 °C

Sadegh Pour-Ali<sup>a</sup>, Ali-Reza Kiani-Rashid<sup>a</sup>, Abolfazl Babakhani<sup>a</sup>, Mohsen Norouzi<sup>b</sup>, Sannakaisa Virtanen<sup>c,\*</sup>

<sup>a</sup> Materials and Metallurgical Engineering Department, Faculty of Engineering, Ferdowsi University of Mashhad, Postal code 91775-1111, Mashhad, Iran

<sup>b</sup> State Key Laboratory of Digital Manufacturing Equipment and Technology, School of Mechanical Science and Engineering, Huazhong University of Science and Technology, Postal code 430074, Wuhan, China

<sup>c</sup> Department of Materials Science, WW4-LKO, University of Erlangen-Nuremberg, Martensstrasse 7, Postal code D-91058, Erlangen, Germany

## ARTICLE INFO

### Keywords:

- A. Stainless steel
- B. TEM
- B. XPS
- C. Oxidation

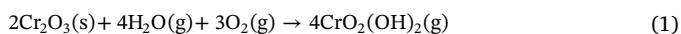
## ABSTRACT

Oxidation behaviour of surface nanocrystallized 321 austenitic stainless steel (SN-321ASS) and its conventional polycrystalline counterpart (CP-321ASS) in O<sub>2</sub> + 10% H<sub>2</sub>O at 1000 °C was comparatively investigated. Uniform dense distribution of high diffusivity paths on the SN-321ASS greatly enhances the Cr and Mn diffusion throughout the oxidation front. Consequently: (i) formation of a thicker Cr-rich inner oxide layer on the SN-321ASS leads to a superior oxidation resistance, (ii) formation of Mn-rich spinel oxide as a uniform intermediate layer interrupts the easy access of oxygen and/or water to the Cr-rich inner oxide layer, thereby reducing the Cr-vaporization.

## 1. Introduction

Austenitic stainless steels (ASSs) are employed in a wide variety of modern applications due to their potentiality to simultaneously withstand corrosive environments and to maintain good mechanical properties [1]. However, high temperature oxidation of ASSs mainly depends on their ability to form a thermally grown, dense, well-adherent and protective Cr-rich  $\alpha$ -(Cr<sub>x</sub>Fe<sub>1-x</sub>)<sub>2</sub>O<sub>3</sub> scale [2–4]. The protectiveness of such scales can be affected by a number of parameters, including the elemental composition [5], oxidation temperature [6,7], grain size [8], surface treatment and preparation [9], presence or absence of water vapour [10,11], and oxygen partial pressure [12]. In general, oxide scales on ASSs are stable, adherent and protective at even above 700 °C in dry oxidising atmospheres. However, the presence of water vapour can influence the process of high temperature oxidation of ASSs by modifying the structural characteristics of the growing oxide scale and the oxidation kinetics [10,12].

Water vapour, which is generally found in the high temperature oxidising environments, reduces the oxidation resistance of ASSs especially at temperatures above 600 °C [6]. This is due to the water vapour reaction with chromia in the scale and production of volatile species by the following reaction:



In addition, oxygen alone can also react with the chromia and generate some volatile species at temperatures above 1000 °C [13,14]:



The formation of volatile oxides and oxy-hydroxides may expedite consumption of the protective oxides [15,16]. In addition, water vapour accelerates the diffusion of oxygen along the grain boundaries by the penetration of hydrogen, hence further promoting the Cr depletion [17,18]. In these cases, the surface scale converts into a non-protective Fe-rich scale and oxidation rate is greatly increased, i.e. “breakaway oxidation” is started. If the overall Cr concentration underneath the oxide scale reaches a level below the required concentration, or no intermediate barrier layer is formed between the Cr-rich inner layer and ASS substrate and/or Fe-rich outer layer, continuous Cr-vaporization will take place [6,18–21]. Several methods have been proposed to overcome these issues and to improve the high temperature resistance of ASSs in humid atmospheres. For instance, Zhongdi et al. [22] showed that minor amount of Al ( $\approx$  2.7 wt.%) in ASSs can promote the formation of a thin Al-rich oxide layer between the substrate and Cr-rich oxide, thereby prohibiting pore formation and Cr-vaporization. Lu et al. [23] claimed that a thin Co-2.4 at.% W coating can effectively block the outward diffusion of Cr ions and this behaviour provides a strong possibility to stop the Cr-vaporization. Reactive element alloying [24], spinel coatings [25], and surface modifications [26] are also among the

\* Corresponding author.

E-mail address: [virtanen@ww.uni-erlangen.de](mailto:virtanen@ww.uni-erlangen.de) (S. Virtanen).

<https://doi.org/10.1016/j.corsci.2018.11.024>

Received 28 July 2018; Received in revised form 20 November 2018; Accepted 22 November 2018

Available online 26 November 2018

0010-938X/ © 2018 Elsevier Ltd. All rights reserved.

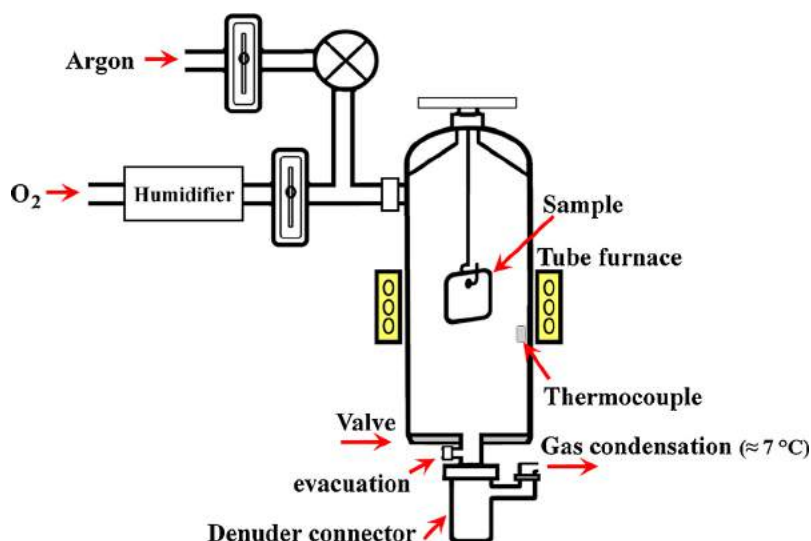


Fig. 1. Simplified schematic of the experimental system for the oxidation tests.

highly recommended methods to reduce the Cr-vaporization in stainless steels at high temperatures.

Apart from the conventional application of surface nanocrystallization (SNC) for improving the mechanical/fatigue properties of stainless steels [27], this method has been successfully employed to improve the high temperature oxidation resistance of ASSs [28]. The idea behind this approach is that the high temperature oxidation is a surface diffusional phenomenon which is greatly dependent on the density of grain boundaries (GBs) as high diffusivity paths [1,29–31]. So, it is expected that enhanced GBs can provide more transport paths for Cr diffusion resulting in an increased selective oxidation of Cr and faster formation of Cr-rich scales. Several previous works have examined the effect of nanocrystallization and grain refinement on the high temperature oxidation performance of ASSs in dry atmospheres, and all of them mentioned the latter scenario as the main mechanism for the increased oxidation resistance of ultrafine grained ASSs [28]. Despite previous research, there is a need for an improved understanding of the effects of SNC on the initial and long-term high temperature oxidation behaviour of ASSs in humid atmospheres. Furthermore, the probable effect(s) of SNC on Cr-vaporization reaction is still an open question and should be studied in detail.

In the present study, initial (1–3 h) and steady-state (5–500 h) oxidation behaviour of coarse-grained 321 ASS and its surface nanocrystallized counterpart were comparatively studied at 1000 °C in the oxygen + 10% water vapour (in vol.%) atmosphere. For the steady-state oxidation, both oxide scale growth and Cr-vaporization were examined. To achieve the goals of this investigation, grazing incidence X-ray diffraction (GI-XRD) analysis, field emission scanning electron microscopy (FE-SEM), glow discharge optical emission spectroscopy (GDOES), transmission electron microscopy (TEM), and X-ray photoelectron spectroscopy (XPS) were used.

## 2. Materials and methods

### 2.1. Materials

The material used in this study was a commercial 321ASS bar (STOOS Co, Switzerland) containing (wt.%) 0.02 C, 0.55 Si, 1.48 Mn, 18.10 Cr, 0.11 Mo, 9.69 Ni, 0.016 P, 0.011 S, 0.46 Ti. The bar with 80 mm in diameter had firstly been solution annealed at 1100 °C for 2 h and then quenched in water. After that, disc-shaped specimens with a thickness of 6.0 mm were sectioned from the bar. These specimens were ground to a final 2000# SiC paper and polished with 6-, 3- and 1-micron water-based diamond suspensions (DP-Suspension P, Struers) to

get a mirror-like surface. Subsequently, these samples were first washed in deionized water, then sonicated in ethanol, and immediately dried with hot air.

### 2.2. Surface nanocrystallization (SNC) process

For the SNC process, severe shot peening (SSP) as a near-surface severe plastic deformation method was applied. In this way, polished disc-shaped specimens were subjected to the SSP using an air blast apparatus (KPS SHOT Co.). SSP was carried out by a peening nozzle with a diameter of 30 mm, mass flow rate of about 8 kg/min and air pressure of 0.30 MPa for 60 min (this condition meets a surface coverage of 1000%). To generate reproducible plastic strains, the shot angle and the distance between the nozzle and top-surface were set to 90° and 400 mm, respectively. This procedure is the optimized output of a series of shot peening processes which have been specified in our previous works [32–35].

### 2.3. Microstructural analysis before the oxidation tests

The cross-section of shot peened specimens for FE-SEM observations was mechanically ground, polished and afterwards etched in a solution containing 2.5 ml H<sub>2</sub>O, 2.5 ml HNO<sub>3</sub> and 5 ml HCl. FE-SEM imaging was provided by a TESCAN MIRA3 field emission scanning microscope at 15 kV. The grazing incidence XRD studies were carried out using an X'Pert Pro MPD X-ray diffraction instrument operated with Cu-K $\alpha$  radiation. The volume fraction of strain-induced martensite ( $V_{I\alpha}$ ) phase in the austenite matrix of different samples was determined by Rietveld refinement using the GSAS software. Dark-field TEM imaging (FEI Tecnai G2) was applied to estimate the average grain size of the treated surface layer.

### 2.4. High temperature oxidation tests

Oxidation tests were conducted in oxygen + 10% water vapour at 1000 °C for different periods of time up to 500 h. Fig. 1 shows the simplified design of apparatus used for the oxidation tests. In this test, square samples of approximately 12 × 12 × 2 mm were prepared from the non-treated and shot peened discs. Before the oxidation tests, temperature calibration was carried out at the test temperature of 1000 °C. Before turning the resistive furnace on, the atmosphere inside the chamber was changed to Ar. After reaching 1000 °C, the chamber was evacuated and subsequently, humid oxygen was introduced into the furnace at a flow rate of 20 cm<sup>3</sup> min<sup>-1</sup>. A humidifier set was used to

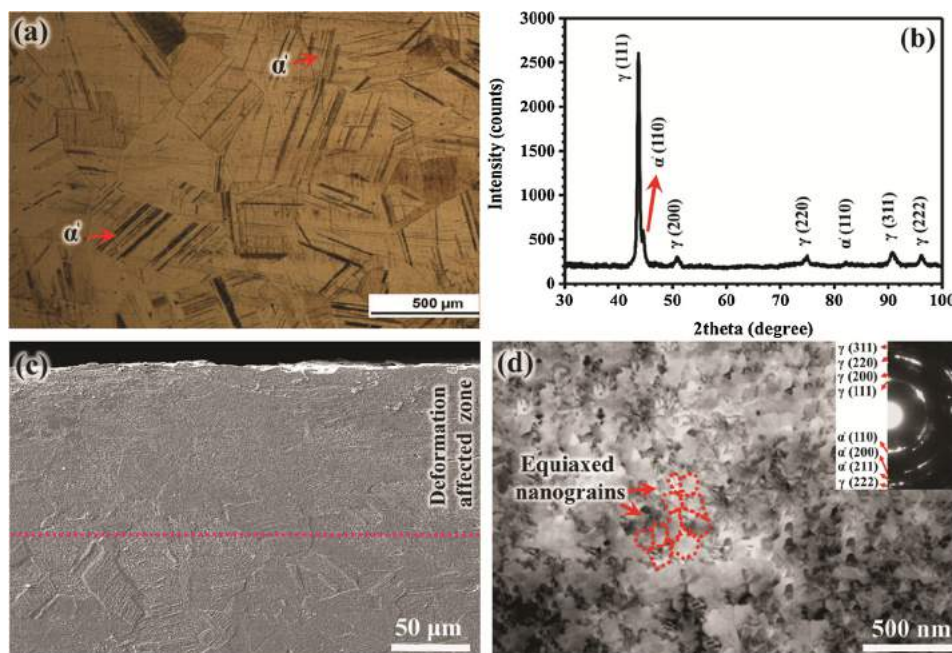


Fig. 2. (a) The original microstructure of the solution-annealed 321SS alloy, (b) corresponding XRD pattern, (c) cross-sectional SEM image of the severely shot peened 321ASS, (d) bright field TEM image and corresponding SAED pattern, from the top-surface of treated 321ASS.

adjust the humidity to 10% in the gas stream. At the outlet of the furnace, a water-containing condenser was installed and its temperature controlled at  $\approx 7^\circ\text{C}$  to condense all Cr volatile species. Experiments were repeated three times for each sample.

## 2.5. Cr-vaporization measurements

As shown in Fig. 1, a silica denuder connector was placed in the lower part of the furnace tube. The inside of the denuder connector was coated with  $\text{Na}_2\text{CO}_3$ , which reacted with the volatile Cr(VI) to form  $\text{Na}_2\text{CrO}_4$  [36]:



The denuder connectors were replaced regularly and rinsed with purified water. After the experiment, the silica connector was cleaned by  $0.1 \text{ mol}\cdot\text{L}^{-1}$  hydrochloric acid and the collected solution was added to the condenser solution which was analysed by inductively coupled plasma (ICP) to measure the amount of volatilized chromium. For all samples, the experimental error on the volatilized mass was determined to be less than  $\pm 10.0\%$ .

## 2.6. Analysis of oxide scales

The surface observation of oxide films on different samples was carried out using FE-SEM (Hitachi SEM FE 4800) with an accelerating voltage of 10 kV. Depending on the thickness of oxide layers on various samples, different analytical methods for the cross-sectional analysis in transient (1–3 h) and steady-state (5–500 h) stages were used. In fact, due to the formation of thicker oxides (more than  $\approx 1 \mu\text{m}$  thick) for the exposures more than 3 h, it was difficult to use TEM because of the limited view of the relevant microstructures which are coarser than the TEM observation. On the other hand, for exposures less than 3 h, the oxide films on the alloy were too thin to be evaluated by FE-SEM.

### 2.6.1. Transient stage (1–3 h)

To determine the chemical state of the surface scales during initial stages of oxidation, XPS (PHI 5000 VersaProbe, Ulvac-PHI) was employed in conjunction with Ar ion beam (3 keV) sputtering. The XPS survey scan and high-energy resolution elemental spectra were

acquired. The energy scale was calibrated by placing the C1s peak at 285 eV. The elemental spectra were fitted using Casa XPS software, with Gaussian-Lorentzian lines and Shirley background type.

A SEM/FIB dual-beam system (FEI Quanta 3D FEG) was applied for the TEM sample preparation. In this way, a layer of platinum was first deposited on an area with a size of  $8 \times 3 \mu\text{m}$  to protect the oxide film during lamella preparation. After that, by using the focused ion beam (FIB) with gallium ion sputtering a wedge-shaped lamella with Pt clad layer ( $\approx 8 \times 3 \times 4 \mu\text{m}$ ) was cut from the oxidised sample. Finally, the lamella was put on a TEM sample grid and thinned to electron transparency by Ga sputtering. This method was adopted from [37]. The prepared lamellas were carefully analysed using two modes of TEM (FEI Tecnai G2): bright field mode for the morphological observations and STEM mode for the composition analyses. During the TEM analysis, EDS line scan was applied to reveal the elemental distribution in the cross-section of samples. In order to measure the thickness of oxide layers, 30 regions of each sample were chosen. Each measuring region was about 30 nm apart from another one.

### 2.6.2. Steady-state stage (5–500 h)

For this group, elementary depth profiles were obtained from the surface of samples using Glow Discharge Optical Emission Spectroscopy (GDOES, GD-Profilier 2). The glow discharge was powered by a 13.56 MHz radio-frequency generator. Moreover, these oxidised samples were analysed cross-sectionally by FE-SEM equipped with an energy dispersive spectrometer (EDS). For the latter purpose, the oxidised samples were gold sprayed and after that, a nickel layer was electrochemically deposited on their surface to protect the oxide scales. Finally, the Ni-electroplated samples were mounted and polished in a way similar to Section 2.1.

## 3. Results

### 3.1. Microstructural characteristics before oxidation

Microstructural characteristics of the as-received 321 ASS and the surface treated one were reported in detail elsewhere [32–35,38,39]. Specifically, Fig. 2 shows these characteristics in the as-received and shot peened 321ASS samples. Fig. 2a and b depict the metallographic

observation of the as-received material and corresponding XRD pattern, respectively. As can be seen, the microstructure consists of austenite ( $\gamma$ ) as the matrix phase and fine needles of  $\alpha'$  ( $V_{\alpha'} \approx 10\%$ ) within the  $\gamma$  grains. Considering the production process of ASSs rods (continuous casting/hot rolling/cold finishing), ASSs should contain some amounts of martensite even after solution-annealing heat treatment. The amount of this phase is normally below 10% [40,41]. This phase is fully re-transformed to the  $\gamma$  phase at temperatures higher than 800 °C [33]. Fig. 2c displays an SEM image from the cross-section of shot peened sample. It is obvious that the microstructural differences between the deformation affected zone and the matrix are distinct; however, there is not a sharp boundary between them. The total thickness of the deformation affected layer is about 120  $\mu\text{m}$ . Fig. 2d also shows the bright field TEM micrograph and corresponding SAED patterns of the microstructure of the top-surface of shot peened sample. A nearly full surface nanocrystallization is observed after the SSP, so that extremely fine and equiaxed nano-grains with random crystallographic orientation and size of 70–75 nm are distributed in the whole microstructure. This microstructural refinement is also reflected in the SAED patterns, where continuous rings appear instead of streak points. The non-treated and shot peened samples are respectively named as conventional polycrystalline 321 austenitic stainless steel (CP-321ASS) and surface nanocrystallized one (SN-321ASS) hereafter.

### 3.2. Surface morphology of oxide films

Fig. 3 shows typical SEM images of the oxide films formed on the CP-321ASS surface after 1, 3, 5, 50, 100 and 500 h exposure. Initially, a fast-growing oxide film is detected (Fig. 3a). This film is made up of fine octahedral oxide particles (size in the range of 0.15 – 0.30  $\mu\text{m}$ ) with some thickening along GBs of the underlying substrate. Moreover, some fine oxide nodules are also observed inside the oxidised grains. The EDS analyses indicate that the oxide film is mainly consisting of Fe, Cr, O, and Mn and oxide nodules are enriched in Fe and O (Fig. S1 in the Supplementary material). With increasing the oxidation time, the oxide nodules rapidly grow and cover the entire surface after 5 h. After 50 h oxidation, in many areas the outer scale cracks and spalls off, and subsequently (Ni, Fe)-rich oxides grow on the spalled area as shown in Fig. S2. It is indisputable that the cracks contribute to the final spallation of the oxide scale. In addition to these features, the formation of coarse polygonal crystals with flat facets (size in the range of 2–18  $\mu\text{m}$ ) is the main surface characteristic after longer exposures (e.g. see Fig. 3f).

In the case of SN-321ASS sample (Fig. 4), no sparse oxide nodules are observed in the early stages of oxidation, instead a uniform and steady growing oxide scale is developed. In fact, the oxide surface is predominantly covered by equiaxial oxide particles and these faceted particles are enlarged as the oxidation time increases (Fig. 4a–c). Moreover, in some areas of the outer oxide of SN-321ASS, microcracking and spallation of the oxide is detected after 50 h oxidation;

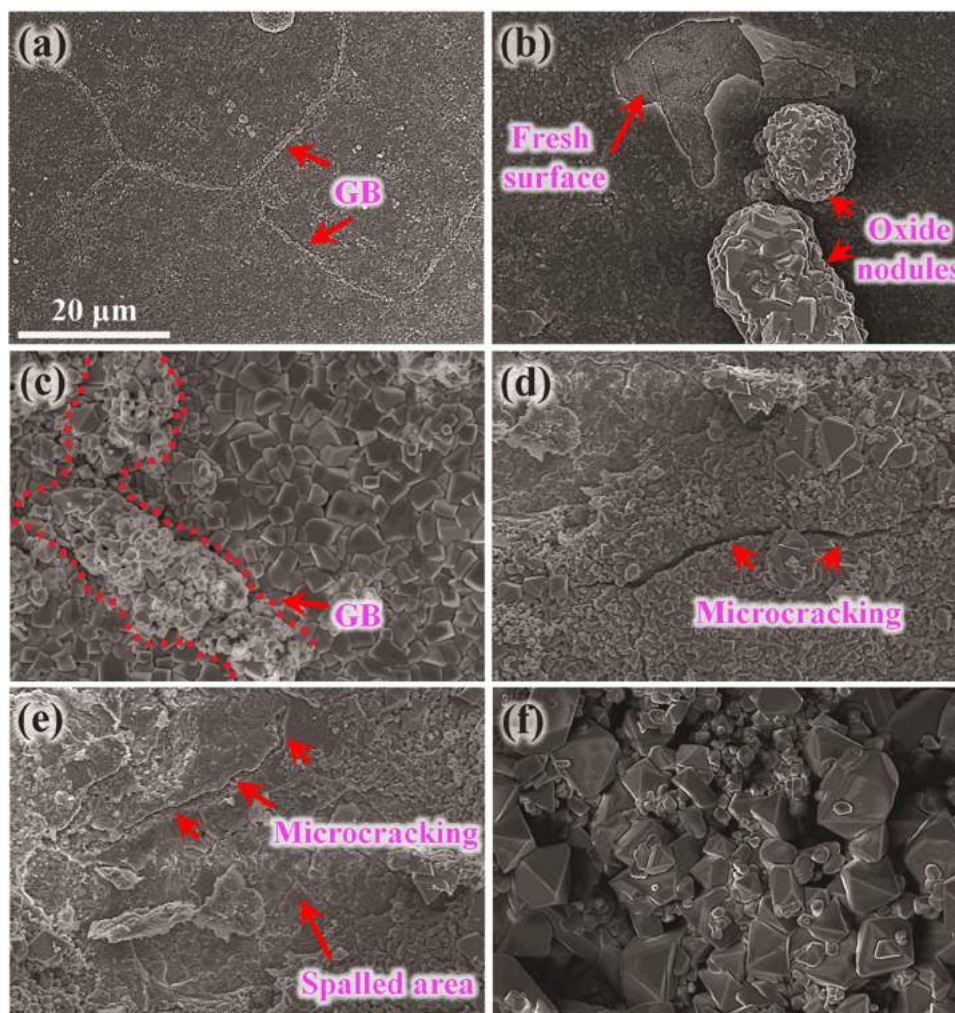


Fig. 3. Surface morphologies of the CP-321ASS sample oxidised in humid oxygen at 1000 °C for different exposure times: (a) 1 h, (b) 3 h, (c) 5 h, (d) 50 h, (e) 100 h, and (f) 500 h.

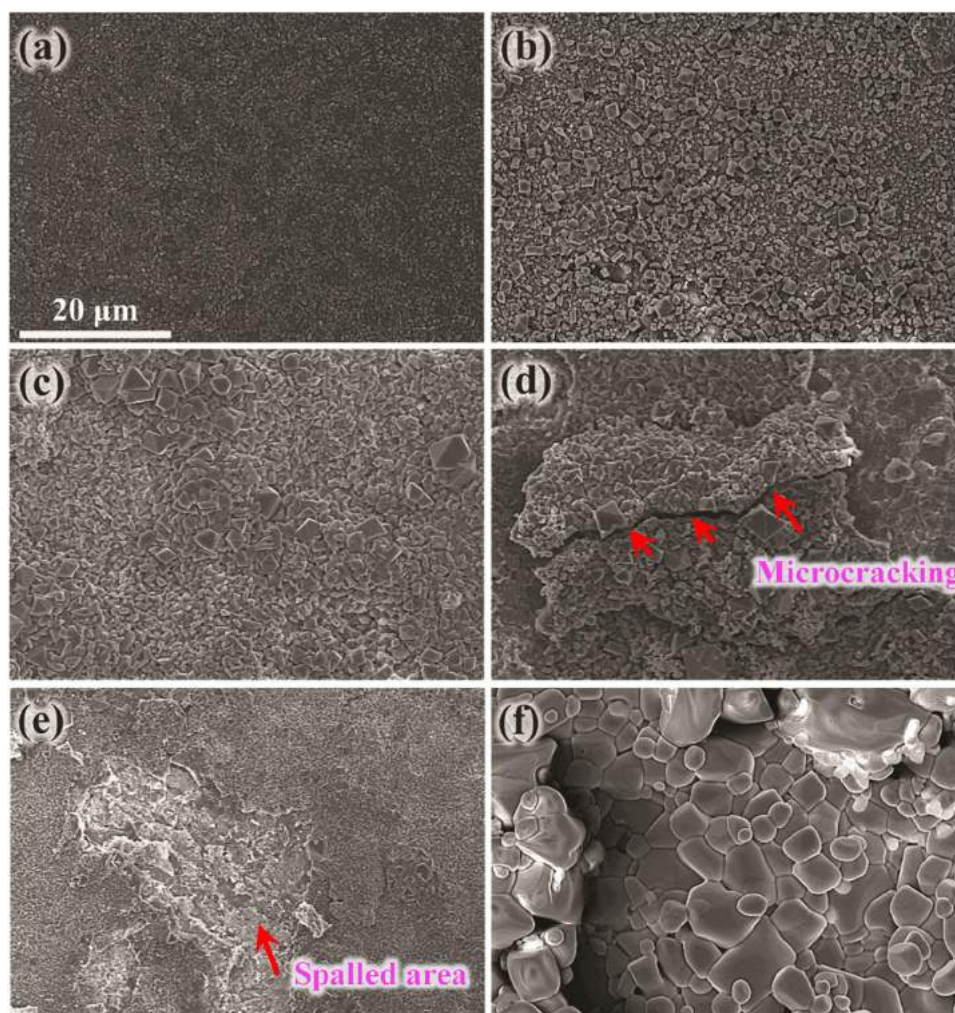


Fig. 4. Surface morphologies of the SN-321ASS sample oxidised in humid oxygen at 1000 °C for different exposure times: (a) 1 h, (b) 3 h, (c) 5 h, (d) 50 h, (e) 100 h, and (f) 500 h.

however, a Cr-rich oxide scale is formed in the spalled areas (Fig. S3). This is an indication of higher supply rate of Cr from the underlying steel to the steel-oxide interface where a large number of GBs serve as “short-circuit” channels for Cr diffusion [6,42].

### 3.3. More detailed analysis for exposure times of 1, 2, and 3 h

Figs. 5–7 show the full survey XPS spectra and high-resolution spectra (binding energy intervals of 0.1 eV) of the major elements obtained at different depths of CP-321ASS and SN-321ASS samples oxidised at 1000 °C in oxygen + 10% water vapour for 1, 2, and 3 h. The results show the presence of chromium in addition to iron, oxygen and carbon on the surface of both samples after 1 h. The appearance of carbon is ubiquitous due to surface contamination (Fig. 5a), and as expected, it disappears after further sputtering (Figs. 6a and 7a). After 2 h of exposure, Ti 2p and Mn 2p peaks are also detected in the XPS survey of SN-321ASS (Fig. 6a); however, the latter peak is not detected for the CP-321ASS sample. In the case of CP-321ASS, both peaks of Ti 2p and Mn 2p appear after 3 h of exposure. This can be a good indication of lower supply rate of these alloying elements in the oxidation front of the CP-321ASS sample. It is notable that although Ni is the third most abundant element in the substrate, it was not detected in the XPS spectra of both kinds of samples even after 3 h of exposure. It is probably due to its lower outward diffusion rates within the substrate and lower oxygen affinity as compared to Fe, Cr, Mn, and Ti [43,44].

The results of the high resolution XPS spectra of Fe 2p clearly show

the enhanced formation of  $\text{Fe}_3\text{O}_4$  at the early stages of oxidation for both samples. Due to the multivalent nature of the Fe in  $\text{Fe}_3\text{O}_4$ , the Fe 2p peak was deconvoluted into the  $\text{Fe}^{2+}$  and  $\text{Fe}^{3+}$  peaks. Since stoichiometric  $\text{Fe}_3\text{O}_4$  can also be expressed to  $\text{FeO}\cdot\text{Fe}_2\text{O}_3$ , the  $\text{Fe}^{2+}:\text{Fe}^{3+}$  ratio should be 1:2. The results of the deconvoluted peaks give  $\text{Fe}^{2+}:\text{Fe}^{3+} = 0.35 \pm 0.02$ ;  $0.65 \pm 0.01$ ; this proportion clearly proves that the Fe is mainly in the form of  $\text{Fe}_3\text{O}_4$  for 1 h exposure. Formation of this oxide is also proved in the high resolution XPS spectra of O 1s (Fig. 5d). The above mentioned proportion significantly deviates from 1:2 for 2 h (only for SN-321ASS) and 3 h (for both samples) exposures which can be attributed to the formation of  $\text{Mn}(\text{Fe,Cr})_2\text{O}_4$  phase [45]. For both CP-321ASS and SN-321ASS,  $\text{Fe}_2\text{O}_3$  content decreases as the exposure time increases and it disappears at 2 h. Yunhui et al. [46] also reported that hematite transforms to other phases through solid state reactions during high temperature humid oxidation. As can be seen from Figs. 5b, 6b and 7b, although both groups of samples show similar Fe-containing species during oxidation, their main difference is the faster formation of  $\text{MnFe}_2\text{O}_4$  in the case of SN-321ASS. Unlike the SN-321ASS, this Mn-rich spinel does not appear after 2 h of exposure in the CP-321ASS sample.

The high resolution XPS spectra of Cr 2p (Figs. 5c, 6c, and 7c) demonstrate the presence of similar components in both CP-321ASS and SN-321ASS samples, most probably  $\text{Cr}_2\text{O}_3$  located at  $576.7 \pm 0.2$  eV [47],  $\text{Cr}(\text{OH})\text{O}$  at  $577.2 \pm 0.2$  eV [46],  $\text{Cr}^{+6}$  species at  $578.8 \pm 0.2$  eV [48], and  $(\text{Fe,Mn})\text{Cr}_2\text{O}_4$  at  $576.0 \pm 0.2$  eV [49]. The latter species appears at 2 h and 3 h exposures for SN-321ASS and

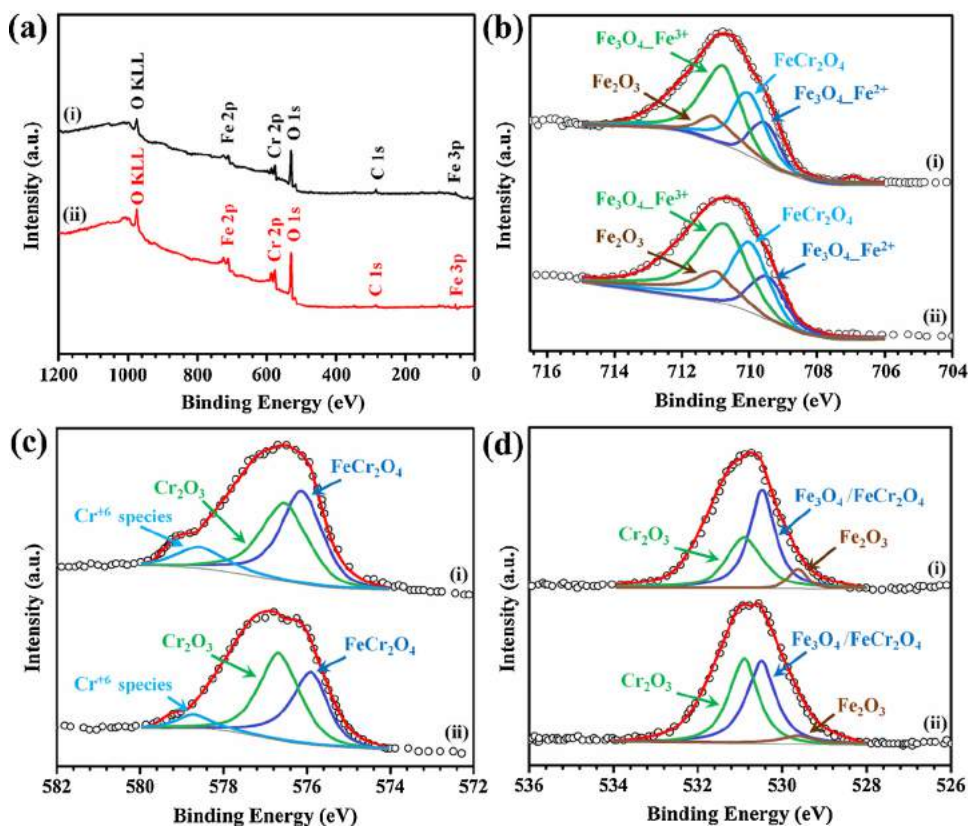


Fig. 5. (a) XPS survey spectra of the oxide films formed on the (i) CP-321ASS and (ii) SN-321ASS, (b) high resolution spectra of Fe 2p<sub>3/2</sub> with their decomposition for the (i) CP-321ASS and (ii) SN-321ASS, (c) high resolution spectra of Cr 2p<sub>3/2</sub> with their decomposition for the (i) CP-321ASS and (ii) SN-321ASS, and (d) XPS O 1s spectra with their decomposition for the (i) CP-321ASS and (ii) SN-321ASS (oxidation at 1000 °C for 1 h).

CP-321ASS samples, respectively. In spite of no notable difference in the type of formed species in both groups of samples, the Cr<sub>2</sub>O<sub>3</sub> concentration in the oxidised SN-321ASS is meaningfully higher than the

CP-321ASS, indicating increased outward diffusion of Cr to the oxidation front as a result of the presence of significant amounts of high diffusivity paths (mainly dislocations and GBs) in the underlying

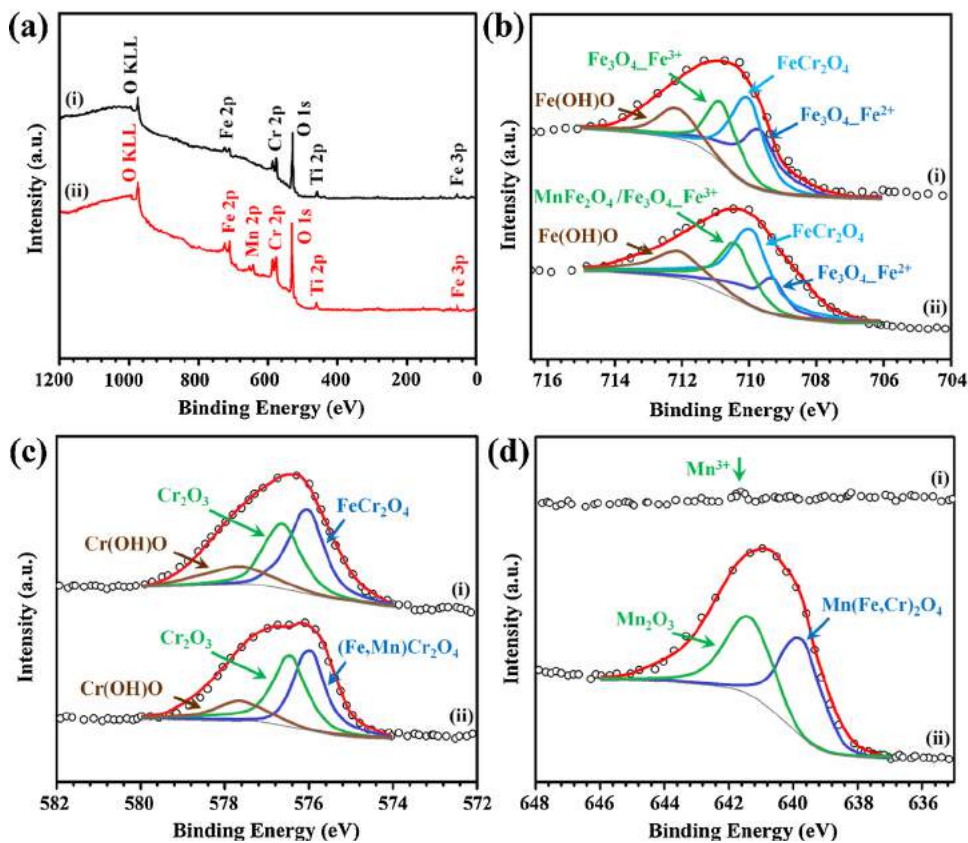


Fig. 6. (a) XPS survey spectra of the oxide films formed on the (i) CP-321ASS and (ii) SN-321ASS, (b) high resolution spectra of Fe 2p<sub>3/2</sub> with their decomposition for the (i) CP-321ASS and (ii) SN-321ASS, (c) high resolution spectra of Cr 2p<sub>3/2</sub> with their decomposition for the (i) CP-321ASS and (ii) SN-321ASS, and (d) high resolution spectra of Mn 2p<sub>3/2</sub> with its decomposition (oxidation at 1000 °C for 2 h).

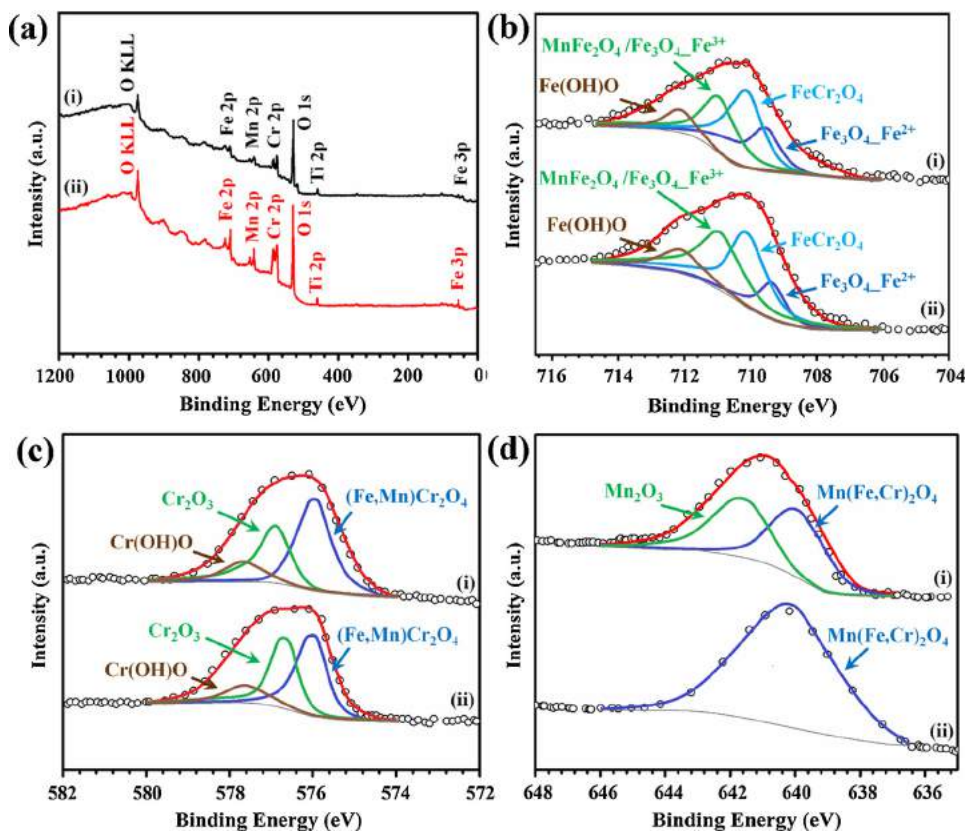


Fig. 7. (a) XPS survey spectra of the oxide films formed on the (i) CP-321ASS and (ii) SN-321ASS, (b) high resolution spectra of Fe 2p<sub>3/2</sub> with their decomposition for the (i) CP-321ASS and (ii) SN-321ASS, (c) high resolution spectra of Cr 2p<sub>3/2</sub> with their decomposition for the (i) CP-321ASS and (ii) SN-321ASS, and (d) high resolution spectra of Mn 2p<sub>3/2</sub> with their decomposition for the (i) CP-321ASS and (ii) SN-321ASS (oxidation at 1000 °C for 3 h).

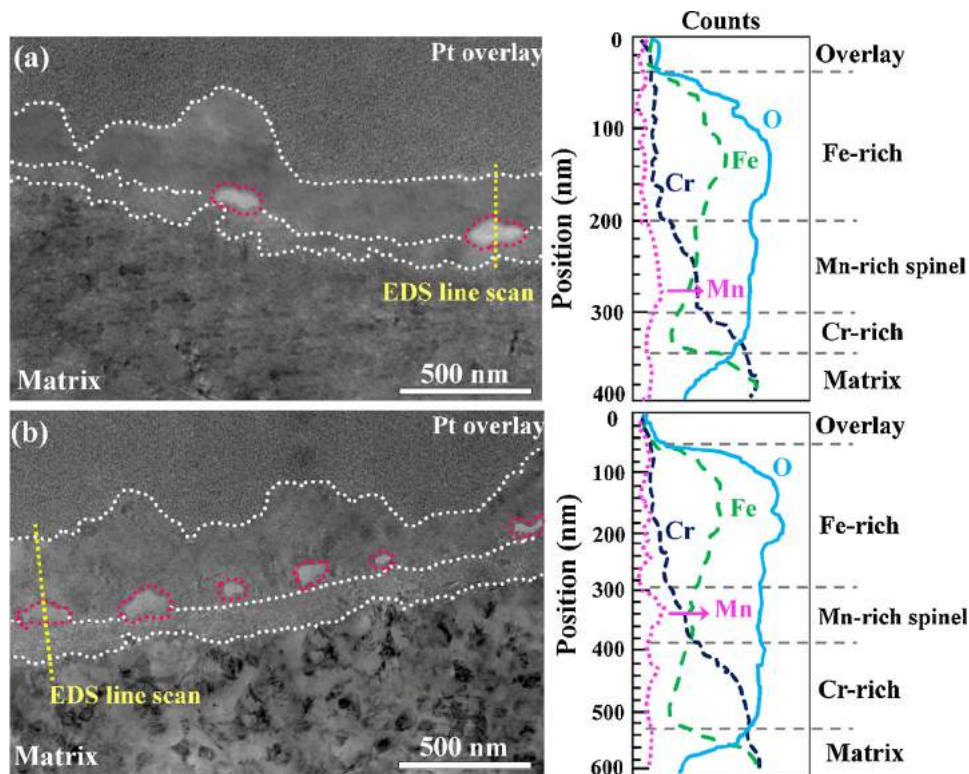


Fig. 8. TEM images of the cross-sectional morphology and corresponding EDS line scan profiles of oxide films grown on (a) CP-321ASS and (b) SN-321ASS after 1 h exposure.

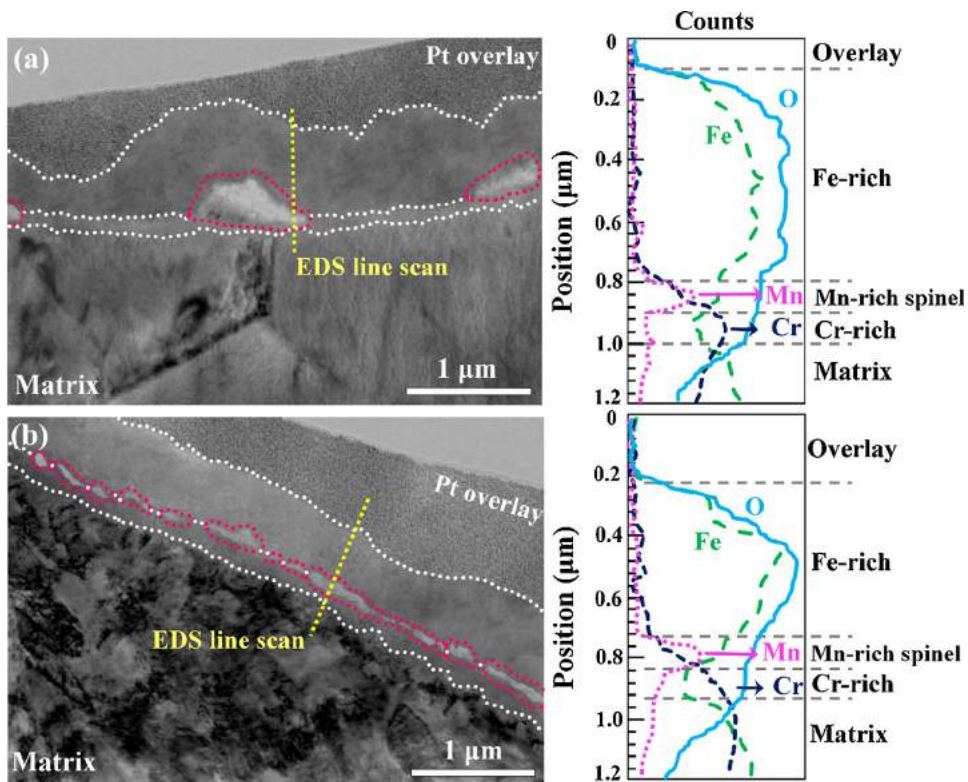


Fig. 9. TEM images of the cross-sectional morphology and corresponding EDS line scan profiles of oxide films grown on (a) CP-321ASS and (b) SN-321ASS after 2 h exposure.

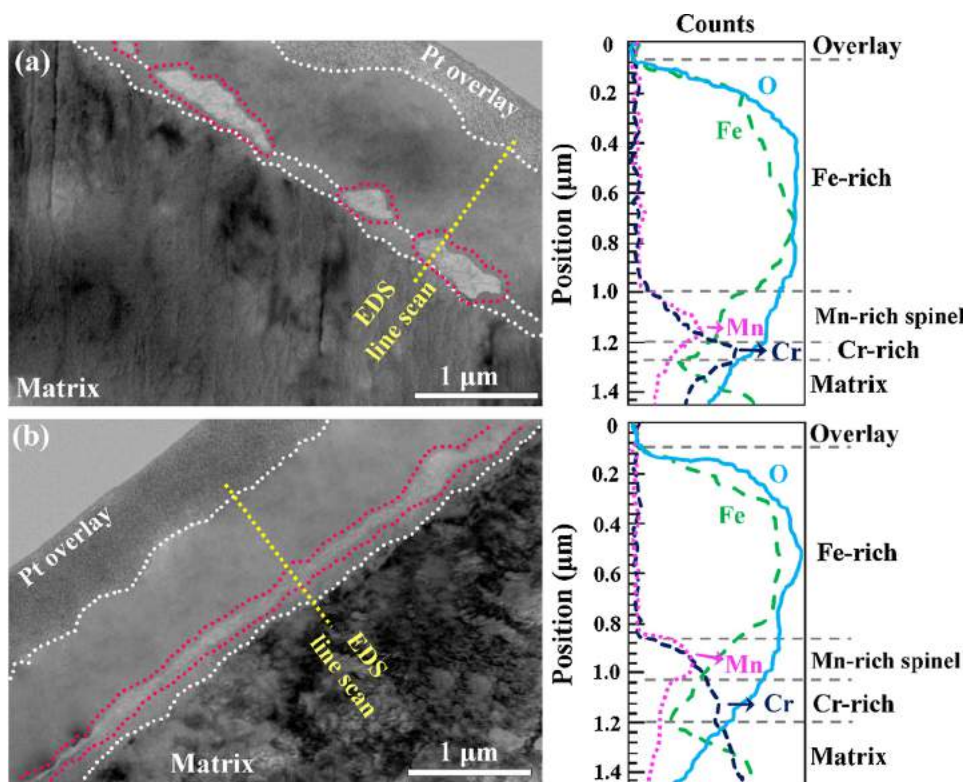


Fig. 10. TEM images of the cross-sectional morphology and corresponding EDS line scan profiles of oxide films grown on (a) CP-321ASS and (b) SN-321ASS after 3 h exposure.

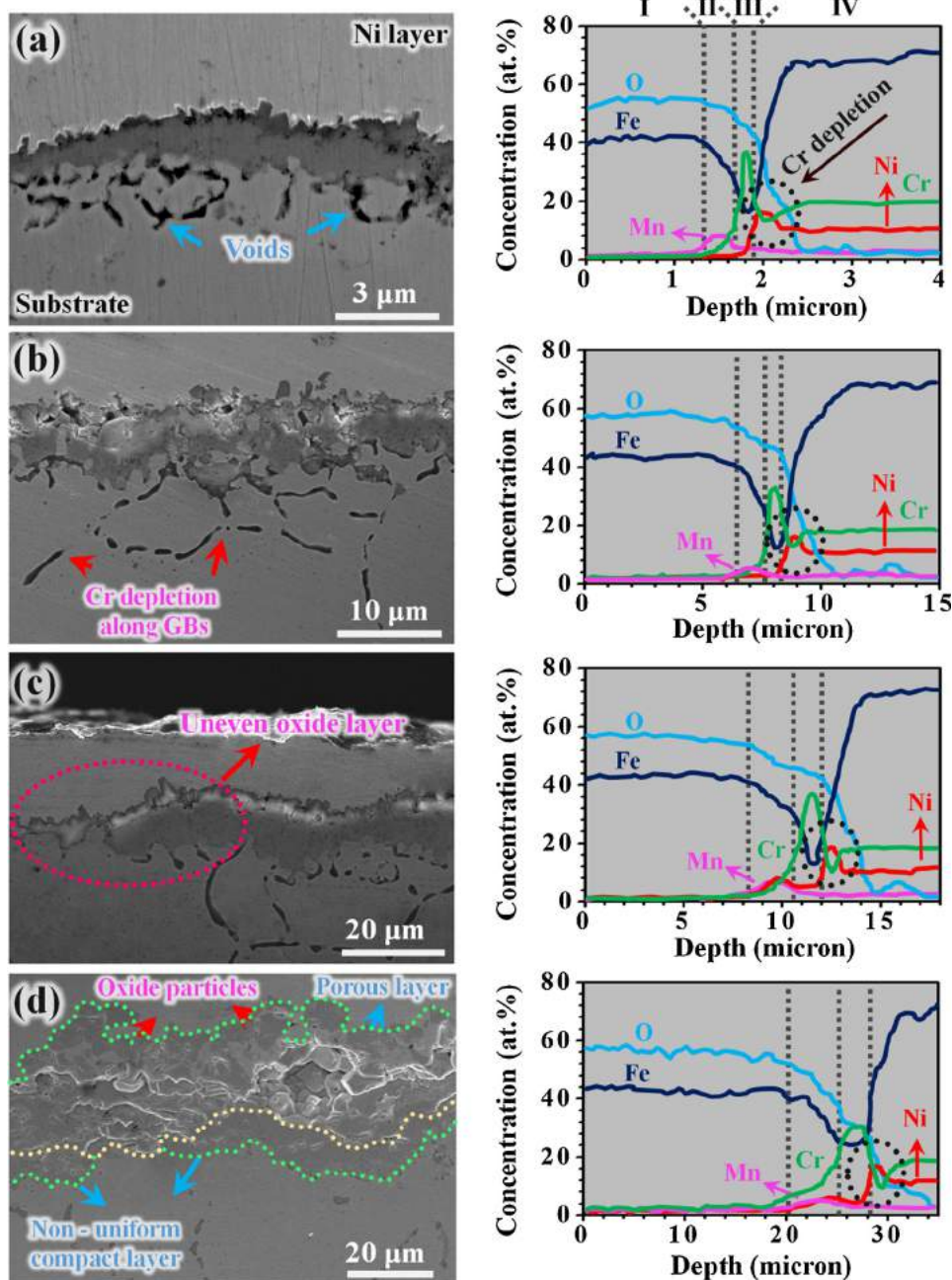


Fig. 11. SEM cross-section and GDOES profiles of oxide scales formed on CP-321ASS after various isothermal oxidation times: (a) 5 h, (b) 20 h, (c) 50 h, and (d) 100 h.

substrate [6,8].

Narrow scans of Mn 2p are displayed in Figs. 6d and 7d. It should be noted that this element does not contribute to the oxide scale of both CP-321ASS and SN-321ASS samples oxidised for 1 h. For 2 h exposure, the signal of Mn 2p for CP-321ASS sample is too weak to be fitted (Fig. 6d) but this element is fitted with two components at  $639.8 \pm 0.1$  eV (probably  $\text{Mn}(\text{Fe},\text{Cr})_2\text{O}_4$ ) and  $641.6 \pm 0.1$  eV (probably  $\text{Mn}_2\text{O}_3$ ) for the SN-321ASS sample. At 3 h exposure, CP-321ASS shows two latter signals with lower intensities; however, the Mn 2p peak is fitted well with only one component at 639.9 eV for the SN-321ASS, which corresponds to the  $\text{Mn}(\text{Fe},\text{Cr})_2\text{O}_4$  spinel oxide.

It is worth to note that Ti oxide has the highest thermodynamic stability among the other constituents of the 321ASS [50]; however, regarding the Ti concentration in the 321ASS substrate, Ti 2p signal with clearly higher intensity for the SN-321ASS sample appears after

2 h exposure (see Fig. S4). Ardigo-Besnard et al. [51] also reported that the  $\text{TiO}_2$  oxide as discrete and fine particles is formed close to the steel/oxide interface during high temperature humid oxidation of Ti-containing stainless steels (see Fig. S5).

Figs. 8–10 display cross-sectional TEM images of the oxide films grown on the SN-321ASS and SN-321ASS samples after 1, 2, and 3 h exposures and their corresponding EDS line scans.

After 1 h (Fig. 8), the oxide film in both samples shows a double-layer structure: considering the XPS and EDS results, an outer layer composed of iron oxides (mainly  $\text{Fe}_3\text{O}_4$ ) and an inner layer made up of chromium oxides (mainly  $\text{Cr}_2\text{O}_3$ ). In some areas between these two distinct layers, Fe–Cr oxides (probably  $\text{FeCr}_2\text{O}_4$  spinel oxide) as fine and discrete oxide particles are also observed, their amount being higher in the SN-321ASS sample. The total thickness of oxide layer in CP-321ASS and SN-321ASS samples is  $343 \pm 196$  nm and

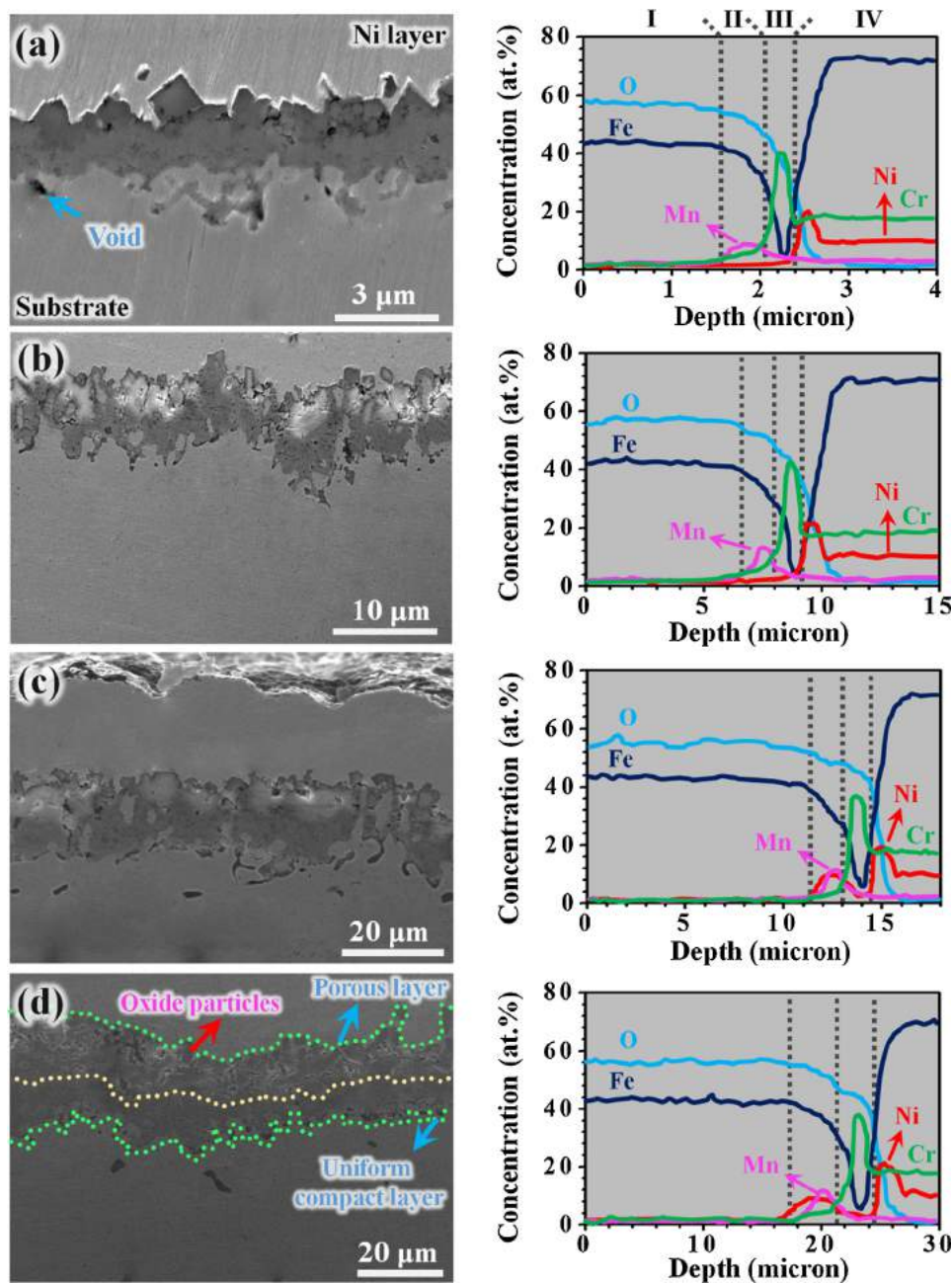


Fig. 12. SEM cross-section and GDOES profiles of oxide scales formed on SN-321ASS after various isothermal oxidation times: (a) 5 h, (b) 20 h, (c) 50 h, and (d) 100 h.

$390 \pm 79$  nm, respectively. The inner layer is Cr-rich, so it plays a more important role in the oxidation kinetics and diffusion of ionic species through the oxide film [28]. This layer in both samples is compact; however, its thickness is more uniform in the case of SN-321ASS ( $\approx 109 \pm 10$  nm) compared with CP-321ASS ( $\approx 86 \pm 39$  nm). The presence of such a thick and uniform Cr-rich inner layer on SN-321ASS can guarantee an improved oxidation behaviour for further exposures [6].

As can be seen from Fig. 9 (2 h exposure), the total thickness of oxide films increases to  $783 \pm 283$  nm for CP-321ASS and  $726 \pm 126$  nm for SN-321ASS. The uniform thickness of the oxide layer on the SN-321ASS sample distinguishes its morphology from the CP-321ASS. This can result from the presence of a uniformly dense distribution of high diffusivity paths on the surface of underlying substrate. Moreover, the intermediate region is getting more distinguishable with exposure time, so that in the case of SN-321ASS, it is not

discrete and appears as a nearly uniform layer. The EDS results show that this middle layer is containing Fe, Cr, Mn, and O, suggesting  $(\text{Fe,Mn})\text{Cr}_2\text{O}_4$  or  $\text{Mn}(\text{Fe,Cr})_2\text{O}_4$  spinel oxides.

With increasing the exposure time of humid oxidation to 3 h (Fig. 10), SN-321ASS shows a more uniform oxide layer compared with CP-321ASS. This uniformity in thickness is observed for the outer (mainly  $\text{Fe}_3\text{O}_4$ ), inner (mainly  $\text{Cr}_2\text{O}_3$ ), and intermediate (Mn-rich spinel oxide) layers. It is worth noting that although after 1 h exposure (as mentioned above), the thickness of the total oxide layer on the CP-321ASS is less than SN-321ASS (higher initial oxidation rate in the SN-321ASS); these conditions are reversed after 3 h of exposure. This value is  $1149 \pm 83$  nm and  $1066 \pm 33.5$  nm for the CP-321ASS and SN-321ASS, respectively. Fast formation of a thick

Cr-rich inner layer and presence of a spinel intermediate layer in the SN-321ASS can be considered as the main reasons for its reduced oxide thickening rate after 3 h and hence to a better protective nature of this

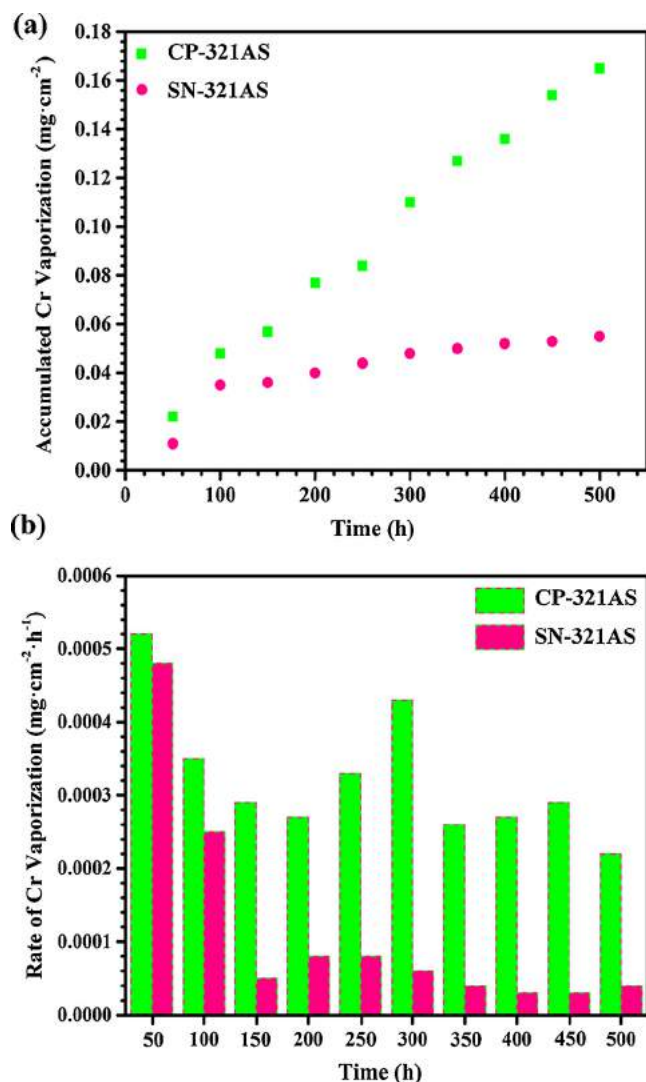


Fig. 13. (a) Accumulated Cr vaporization as a function of time, and (b) rate of Cr-vaporization as a function of time for the CP-321ASS and SN-321ASS samples.

scale (Fig. 10).

From the EDS results, two more points should also be considered:

(i) Severe Cr depletion in the subsurface layers of CP-321ASS: Comparing the Cr line scans of CP-321ASS and SN-321ASS (especially after 3 h) clearly shows that the CP-321ASS suffers from severe Cr depletion at the steel/oxide interface. This phenomenon can significantly affect its resistance to breakaway oxidation [52]. In contrast, it can be claimed that enhanced grain boundary diffusion in the SN-321ASS prevented the Cr depletion due to the Cr consumption by oxidation and simultaneously by Cr-vaporization.

(ii) Ti as a minor alloying element: Although its oxides are more stable than other existing oxides in both group of oxides [50], it stays in the inner oxide layer without noticeable outward diffusion.

### 3.4. Oxidation for the exposure times longer than 3 h

Figs. 11 and 12 show the cross-sectional microstructure and GDOES profile of the oxide scales formed on the CP-321ASS and SN-321ASS samples at different exposure times (up to 100 h). GDOES profiles clearly show that the oxides on both samples show a trend similar to the 3 h exposure i.e. an outer oxide (Fe-rich oxide, mainly Fe<sub>3</sub>O<sub>4</sub>, “I” region), an intermediate oxide (spinel oxide, “II” region), and an inner oxide (Cr-rich, mainly Cr<sub>2</sub>O<sub>3</sub>, “III” region). This behaviour is followed

even during longer exposure times.

For 5 h exposure, both groups show comparable elemental profiles within the oxide layer (except Cr); however, enhanced formation of voids beneath the oxide layer of CP-321ASS sample distinguishes its oxidation behaviour from the SN-321ASS one. The formation of these voids can be attributed to the Kirkendall effect that happened due to outward diffusion of alloying elements (especially Cr). As can be seen from GDOES results, Cr depletion at the steel/oxide interface is a proof of this claim. In the case of SN-321ASS, not only a nearly void-free region beneath the oxide layer is observed but a higher Cr content inner oxide layer is also formed. This shows that the presence of large amounts of crystallographic defects (mainly GBs and dislocations) supplies high amounts of Cr for the oxidation front and consequently Cr depletion below the oxide scale is negligible (for instance, see Fig. 12a). The void formation (Cr-depletion) at the steel/oxide interface and below the oxide layer of CP-321ASS sample intensifies as oxidation proceeds (Fig. 11b–d). This phenomenon can severely affect the oxidation resistance of CP-321ASS. As reported by Zhongdi et al. [22], these voids merge together during longer exposures, form big cracks in the oxide scale, and finally chipping of the scale and breakaway oxidation takes place. This failure process is associated with the formation of uneven and non-uniform oxide layers. Such layers are observed in the case of CP-321ASS sample after 50 h exposure (Fig. 11c). For the longer exposures (e.g. 100 h), the oxide layers morphologically consist of two parts: outer porous layer (Fe-rich oxide) and inner compact layer (Cr-rich and spinel oxides). Since the outer layer is porous and somewhat powdery, accurate evaluation of the cross-section of these oxides is not feasible after 100 h (see Fig. S6). As can be observed in Figs. 11d and 12d, the inner layer is more uniform and thicker in the case of SN-321ASS, indicating higher oxidation resistance compared with CP-321ASS sample SS [30]. Based on GDOES results, CP-321ASS suffers from severe Cr-depletion even after 100 h (Fig. 11d); however, this phenomenon is not significant for SN-321ASS (Fig. 12d). In addition to the Kirkendall effect, Cr-vaporization may take place during the humid oxidation. This phenomenon should account for the void formation.

The measured amount of Cr vaporized as volatile Cr (VI) species for CP-321ASS and SN-321ASS is shown in Fig. 13a. Based on the data presented in this figure, Cr-vaporization of the CP-321ASS is significantly higher than for the SN-321ASS for all exposure times. To compare the kinetics of vaporization, the rate of Cr-vaporization as a function of time during isothermal exposure was calculated as illustrated in Fig. 13b. A significantly higher rate of Cr-vaporization is observed for CP-321ASS sample, which may correspond with the free access of water and/or oxygen to the chromia layer (according to Eqs. (1) and (2)). Inspection of Fig. 13b reveals a considerable decrease in the Cr-vaporization rate of SN-321ASS after 150 h.

For a better understanding of the elemental distribution in the oxide scales of coarse- and nano-grained substrates, cross-sectional EDS mapping was carried out. Fig. 14 depicts the EDS mapping of the CP-321ASS and SN-321ASS samples after 150 h exposure. In line with the GDOES results, oxide layers (“I”, “II”, and “III”) can be distinguished from this elemental mapping. Additionally, the distribution of different elements is also recognizable. Comparing the EDS mappings of CP-321ASS and SN-321ASS samples shows that the intermediate layer for SN-321ASS is uniformly enriched in Fe, Cr, Mn, and Ni oxide (most probably Mn(Fe,Cr)<sub>2</sub>O<sub>4</sub> or Fe(Cr,Ni)<sub>2</sub>O<sub>4</sub> [9,53]) which interrupts the outer (Fe-rich) and inner (Cr-rich) oxide layers. In contrast, some local and discontinuous enrichment of above elements is observed for the CP-321ASS.

## 4. Discussion

In the present paper, oxidation behaviour of CP-321ASS and SN-321ASS samples in humid oxygen at 1000 °C is comparatively investigated. The SN-321ASS sample shows an improved high temperature oxidation performance due to the formation of Cr-rich oxides with

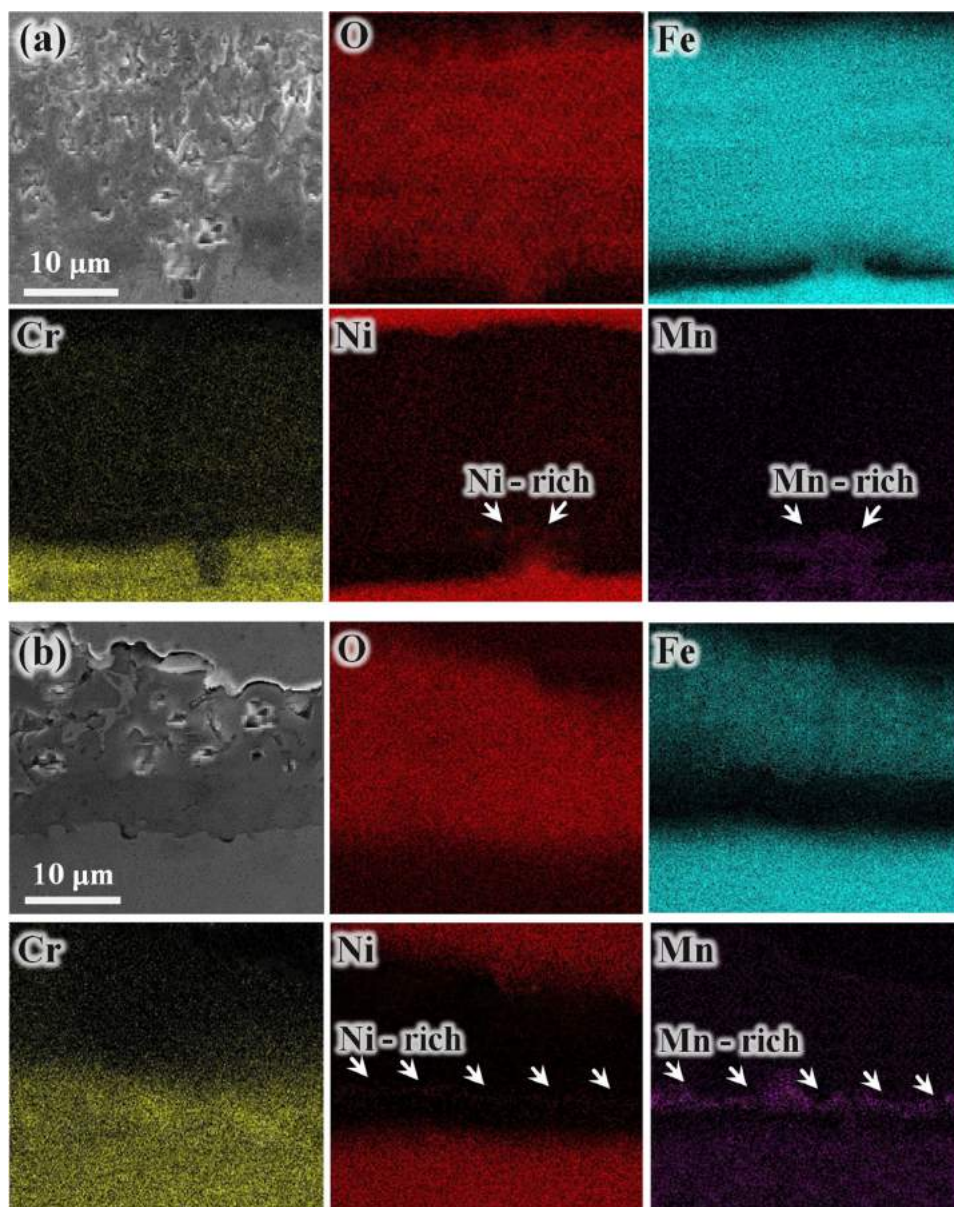


Fig. 14. EDS mapping of the cross-section samples of (a) CP-321ASS and (b) SN-321ASS subjected to  $O_2 + 10\% H_2O$  at  $1000^\circ C$  for 150 h.

high uniformity in thickness, while scales formed on the CP-321ASS are not able to protect substrate as well as the scales on SN-321ASS. CP-321ASS suffers from severe spallation after only 50 h oxidation. In the following sections, oxidation mechanisms are discussed and a physical model is presented to elucidate the effect of SNC on the oxidation behaviour and Cr-vaporization of 321ASS alloy.

#### 4.1. On the oxidation mechanism of 321ASS and effect of SNC on it

In the initial stage of oxidation, all the elements in the 321ASS have equal opportunity to react with oxygen and to produce oxide. Among the most abundant elements in the alloy (i.e. Fe, Cr, and Ni), oxygen affinity for Cr is significantly higher than Fe and Ni. Hence, oxygen reacts with Cr and subsequently a Cr-rich inner oxide layer (mainly  $Cr_2O_3$ ) is formed. In the case of SN-321ASS, presence of large number of high diffusivity paths (GBs and dislocations) leads to a higher supply rate of Cr in the oxidation front, and consequently a thicker inner layer with higher concentration of Cr is formed. In addition, due to the uniform distribution of high diffusivity paths on the surface layers of SN-321ASS, the oxide film is more uniform in thickness as compared

with the CP-321ASS one. Once the thickness of the inner oxide layer reaches a critical value [53], it prevents the underlying substrate from directly contacting with oxygen and the oxidation kinetics is controlled by diffusion of metallic cations through the oxide layer. The diffusion coefficients ( $D$ ) decrease in the order  $D_{Mn} > D_{Fe} > D_{Ni} > D_{Cr}$  in the Cr-rich inner layer [54,55]. Considering the high concentration of Fe at the steel/oxide interface, this element diffuses as iron cations towards the oxide/atmosphere interface through the Cr-rich oxide film. In this region, Fe reacts with oxygen and the outer Fe-rich oxide film (mainly  $Fe_3O_4$ ) is produced. The thicker and more protective Cr-rich inner layer formed on the SN-321ASS can block the outward diffusion of Fe ions and prevent further formation of the Fe-containing outer oxide layer (Fig. 10). Comparing Figs. 11 and 12 reveals that this fact can also influence the long-term oxidation behaviour of 321ASS.

Along with the outward diffusion of Fe ions, steel/oxide interface is gradually enriched in two main elements: Mn and Ni. As supported by XPS and TEM results, after the formation of Cr-rich inner and Fe-rich outer oxide layers, outward diffusion of Mn is probably the most important step in humid oxidation of 321ASS. Since Mn ions have high solubility/diffusivity in the  $Cr_2O_3$  oxide, the formation of its spinel

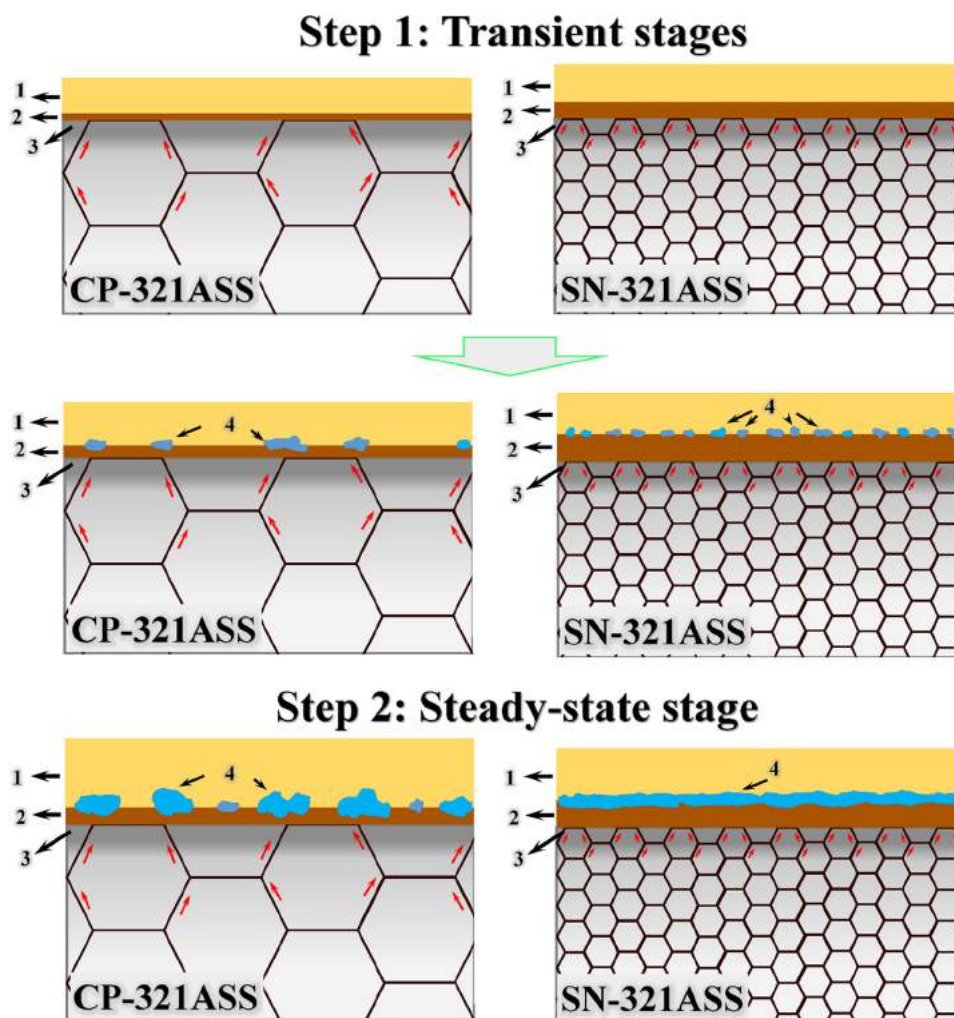


**Fig. 15.** Schematic diagram illustrating oxidation of the CP-321ASS and SN-321ASS in  $O_2 + 10\% H_2O$  at  $1000\text{ }^\circ\text{C}$ : (1) Fe-rich outer oxide layer, (2) Cr-rich inner oxide layer, (3) sub-scale region enriched in Ni, and (4) Mn-rich spinel oxide.

(most probably  $Mn(Cr,Fe)_2O_4$ ) as an intermediate layer between the Cr-rich and Fe-rich layers is plausible (Figs. 7, 10 and 14). Thermodynamically, the formation of  $Mn(Cr,Fe)_2O_4$  can be related to the following solid-state reactions [22,56,57]:



Nickel enrichment at the steel/oxide interface was also observed in the present study. Due to the lowest oxygen affinity of Ni among all the constituents of 321ASS, this element is the least likely to be oxidised. Additionally, its diffusion rate is less than Fe, Cr, and Mn. Consequently; during initial stages of oxidation, Ni does not take part in the oxidation reactions and will be mainly left at the steel/oxide interface. For longer exposures (e.g. 150 h i.e. Fig. 14), minor outward diffusion of this element leads to the formation of Fe-Ni spinel oxide particles between the Cr-rich inner and Fe-rich outer layers.

Although similar Mn-rich spinels are observed in the oxide films

formed on both CP-321ASS and SN-321ASS samples, their distributions are completely different. Similar to what stated for Cr and Fe, the higher density of high diffusivity paths which uniformly are distributed throughout the surface of SN-321ASS, provide enhanced amounts of Mn at nearly all areas of steel/oxide interface. These elements are prone to diffuse across the Cr-rich inner layer, take part in the solid state reactions, and finally form a uniform Mn-rich spinel oxide as an intermediate layer. In contrast, considering the surface grain size of CP-321ASS ( $\approx 380\text{ }\mu\text{m}$  at  $25\text{ }^\circ\text{C}$ ), it can be claimed that Mn mainly reaches the steel/oxide interface through the large angle GBs. In this way, Mn-rich spinel oxide appears with a very sparse distribution between the Cr-rich inner and Fe-rich outer layers. It is worth noting that coarsening of the nanocrystalline surface grains would take place at high temperatures; however, our previous work suggested that SN-321ASS shows a good thermal stability so that its top-surface grain size is several orders of magnitude smaller than the CP-321ASS even after 10 h vacuum annealing at  $1000\text{ }^\circ\text{C}$  [33]. Fig. 15 presents a physical mechanism of oxidation process in the CP-321ASS and SN-321ASS samples.

#### 4.2. Effect of SNC on the Cr-vaporization from 321ASS

Based on a report by Pakshith et al. [58], higher Mn contents leads to a reduced Cr-vaporization rate. They claimed that it is necessary to make the supply of Mn from the underlying substrate to the steel/oxide interface high enough to form a continuous Mn-rich spinel on the

chromia layer. This layer interrupts the direct access of water and/or oxygen to the Cr-rich inner layer, and consequently reduces the Cr-vaporization. In fact, adding more Mn is a normal solution to improve the resistance of stainless steels to Cr-vaporization [59]. Increasing the density of GBs and dislocations (i.e. high diffusivity paths) by SNC can also be considered as an alternative way to provide abundant amounts of Mn at the steel/oxide interface. As previously shown in this work, providing higher amounts of Mn in the oxidation front of SN-321ASS leads to the formation of a continuous and uniform Mn-rich spinel oxide intermediate layer on the Cr-rich inner layer (Fig. 14). This layer cuts off the water and/or oxygen access to the Cr-rich inner layer and decreases the Cr-vaporization rate (according to the Eqs. (1) and (2)).

## 5. Conclusions

From this study, oxidation behaviour of surface nanocrystallized 321 ASS (SN-321ASS) and coarse-grained one (CP-321ASS) in  $O_2 + 10\% H_2O$  at  $1000^\circ C$ , following conclusions can be drawn:

- (1) Oxide films with nearly similar compositions form on the CP-321ASS and SN-321ASS. Both samples show a Fe-rich outer oxide and a Cr-rich inner oxide as continuous layers. The main difference in the configuration of oxide films is related to the formation of Mn-rich spinel oxides. In the SN-321ASS, the Mn-rich spinel oxide appears as a continuous and uniform intermediate layer between two mentioned layers; however, this spinel oxide is formed between the inner Cr-rich and outer Fe-rich oxide layers as separated and sporadic particles in the CP-321ASS. It is notable that the valence state of elements in the oxide film is not influenced by the surface nanocrystallization.
- (2) Enhanced outward diffusion of Cr due to the presence of a large number of high diffusivity paths in the surface layers of underlying substrate (i.e. GBs and dislocations) guarantees the formation of a thicker Cr-rich inner oxide layer with high uniformity for the SN-321ASS sample.
- (3) Ni enrichment was observed at the steel/oxide interface for both CP-321ASS and SN-321ASS. The concentration of Ni at the steel/oxide interface of SN-321ASS was higher than for the CP-321ASS one.
- (4) In the case of SN-321ASS, the presence of a uniform Mn-rich spinel oxide intermediate layer on Cr-rich inner layer leads to a reduced Cr-vaporization rate for the long exposures. In contrast, CP-321ASS suffers from a continuous vaporization with a rate of several times higher than for the SN-321ASS one.
- (5) Unlike the SN-321ASS sample, many voids are created due to the Kirkendall effect and Cr-vaporization underneath the oxide film formed on the CP-321ASS.

## Acknowledgements

The authors would like to appreciate the support from the Erlangen-Nuremberg University (LKO, FAU, Germany), Huazhong University of Science and Technology (HUST, China), and Ferdowsi University of Mashhad (FUM, Iran) (3/39325). Dr. Nhat Truong Nguyen and Mr. Wenqian Zhang are greatly acknowledged for their help in practical work. The authors also thank Mr. Sina Hejazi, Mr. Martin Weiser, Ms. Shiva Mohajernia, Dr. Saeed Abbasizadeh, Mr. Hashem Teimourinejad, and Mr. Afshin Nazarnejatizadeh for valuable discussions.

## Appendix A. Supplementary data

Supplementary material related to this article can be found, in the online version, at doi:<https://doi.org/10.1016/j.corsci.2018.11.024>.

## References

- [1] S.G. Wang, M. Sun, H.B. Han, K. Long, Z.D. Zhang, The high-temperature oxidation of bulk nanocrystalline 304 stainless steel in air, *Corros. Sci.* 72 (2013) 64–72, <https://doi.org/10.1016/j.corsci.2013.03.008>.
- [2] M. Peruzzo, T.D. Beux, M.F.C. Ordoñez, R.M. Souza, M.C.M. Farias, High-temperature oxidation of sintered austenitic stainless steel containing boron or yttria, *Corros. Sci.* (2017), <https://doi.org/10.1016/j.corsci.2017.09.002>.
- [3] Z. Li, Z. Cai, W. Yang, X. Shen, G. Xue, M. Zhu, Characterization and corrosion behaviour of F6NM stainless steel treated in high temperature water, *Appl. Surf. Sci.* 435 (2018) 312–319, <https://doi.org/10.1016/j.apsusc.2017.11.089>.
- [4] D. Zou, Y. Zhou, X. Zhang, W. Zhang, Y. Han, High temperature oxidation behaviour of a high Al-containing ferritic heat-resistant stainless steel, *Mater. Charact.* 136 (2018) 435–443, <https://doi.org/10.1016/j.matchar.2017.11.038>.
- [5] F. Riffard, H. Buscaill, E. Caudron, R. Cuffe, C. Issartel, S. El Messki, S. Perrier, A New interpretation of the “breakaway” oxidation behaviour observed at high temperature on 304 stainless steel, *Mater. Sci. Forum*, Trans Tech Publ, (2004), pp. 175–182, <https://doi.org/10.4028/www.scientific.net/MSF.461-464.175>.
- [6] X. Peng, J. Yan, Y. Zhou, F. Wang, Effect of grain refinement on the resistance of 304 stainless steel to breakaway oxidation in wet air, *Acta Mater.* 53 (2005) 5079–5088, <https://doi.org/10.1016/j.actamat.2005.07.019>.
- [7] D. Li, Q. Dai, X. Cheng, R. Wang, Y. Huang, High-temperature oxidation resistance of austenitic stainless steel Cr18Ni11Cu3Al3MnNb, *J. Iron Steel Res. Int.* 19 (2012) 74–78, [https://doi.org/10.1016/S1006-706X\(12\)60103-4](https://doi.org/10.1016/S1006-706X(12)60103-4).
- [8] L. Liu, Z. Yang, C. Zhang, M. Ueda, K. Kawamura, T. Maruyama, Effect of grain size on the oxidation of Fe-13Cr-5Ni alloy at 973K in Ar-21vol% $O_2$ , *Corros. Sci.* 91 (2015) 195–202, <https://doi.org/10.1016/j.corsci.2014.11.020>.
- [9] S. Cissé, L. Laffont, B. Tanguy, M.-C. Lafont, E. Andrieu, Effect of surface preparation on the corrosion of austenitic stainless steel 304L in high temperature steam and simulated PWR primary water, *Corros. Sci.* 56 (2012) 209–216, <https://doi.org/10.1016/j.corsci.2011.12.007>.
- [10] E.J. Opila, N.S. Jacobson, D.L. Myers, E.H. Copland, Predicting oxide stability in high-temperature water vapour, *Jom* 58 (2006) 22–28, <https://doi.org/10.1007/s11837-006-0063-3>.
- [11] H. Asteman, J.-E. Svensson, L.-G. Johansson, Oxidation of 310 steel in  $H_2O/O_2$  mixtures at  $600^\circ C$ : the effect of water-vapour-enhanced chromium evaporation, *Corros. Sci.* 44 (2002) 2635–2649, [https://doi.org/10.1016/S0010-938X\(02\)00056-2](https://doi.org/10.1016/S0010-938X(02)00056-2).
- [12] H. Asteman, J.-E. Svensson, M. Norell, L.-G. Johansson, Influence of water vapour and flow rate on the high-temperature oxidation of 304L; effect of chromium oxide hydroxide evaporation, *Oxid. Met.* 54 (2000) 11–26, <https://doi.org/10.1023/A:1004642310974>.
- [13] A. Yamauchi, K. Kurokawa, H. Takahashi, Evaporation of  $Cr_2O_3$  in atmospheres containing  $H_2O$ , *Oxid. Met.* 59 (2003) 517–527, <https://doi.org/10.1023/A:1023671206976>.
- [14] G.R. Holcomb, D.E. Alman, The effect of manganese additions on the reactive evaporation of chromium in Ni-Cr alloys, *Scr. Mater.* 54 (2006) 1821–1825, <https://doi.org/10.1016/j.scriptamat.2006.01.026>.
- [15] D.J. Young, B.A. Pint, Chromium volatilization rates from  $Cr_2O_3$  scales into flowing gases containing water vapour, *Oxid. Met.* 66 (2006) 137–153, <https://doi.org/10.1007/s11085-006-9030-1>.
- [16] J. Yuan, W. Wang, H. Zhang, L. Zhu, S. Zhu, F. Wang, Investigation into the failure mechanism of chromia scale thermally grown on an austenitic stainless steel in pure steam, *Corros. Sci.* 109 (2016) 36–42, <https://doi.org/10.1016/j.corsci.2016.03.021>.
- [17] S. Jianian, Z. Longjiang, L. Tiefan, High-temperature oxidation of Fe-Cr alloys in wet oxygen, *Oxid. Met.* 48 (1997) 347–356, <https://doi.org/10.1007/BF01670507>.
- [18] H. Asteman, J.-E. Svensson, L.-G. Johansson, M. Norell, Indication of chromium oxide hydroxide evaporation during oxidation of 304L at 873 K in the presence of 10% water vapour, *Oxid. Met.* 52 (1999) 95–111, <https://doi.org/10.1023/A:1018875024306>.
- [19] A. Col, V. Parry, C. Pascal, Oxidation of a Fe-18Cr-8Ni austenitic stainless steel at  $850^\circ C$  in  $O_2$ : microstructure evolution during breakaway oxidation, *Corros. Sci.* 114 (2017) 17–27, <https://doi.org/10.1016/j.corsci.2016.10.029>.
- [20] C. Pascal, V. Parry, E. Fedorova, M. Braccini, P. Chemelle, N. Meyer, D. Oquab, D. Monceau, Y. Wouters, M. Mantel, Breakaway oxidation of austenitic stainless steels induced by alloyed sulphur, *Corros. Sci.* 93 (2015) 100–108, <https://doi.org/10.1016/j.corsci.2015.01.007>.
- [21] C. Boulesteix, F. Pedraza, Characterisation of aluminium diffusion coatings elaborated on austenitic stainless steels and on ferritic-martensitic steels, *Surf. Coat. Technol.* 339 (2018) 27–36, <https://doi.org/10.1016/j.surfcoat.2018.01.086>.
- [22] Z. Yu, M. Chen, C. Shen, S. Zhu, F. Wang, Oxidation of an austenitic stainless steel with or without alloyed aluminum in  $O_2 + 10\% H_2O$  environment at  $800^\circ C$ , *Corros. Sci.* 121 (2017) 105–115, <https://doi.org/10.1016/j.corsci.2017.03.015>.
- [23] L. Gan, H. Murakami, I. Saeki, High temperature oxidation of Co-W electroplated type 430 stainless steel for the interconnect of solid oxide fuel cells, *Corros. Sci.* 134 (2018) 162–168, <https://doi.org/10.1016/j.corsci.2018.02.026>.
- [24] N. Shaigan, W. Qu, D.G. Ivey, W. Chen, A review of recent progress in coatings, surface modifications and alloy developments for solid oxide fuel cell ferritic stainless steel interconnects, *J. Power Sources* 195 (2010) 1529–1542, <https://doi.org/10.1016/j.jpowsour.2009.09.069>.
- [25] W. Qu, L. Jian, J.M. Hill, D.G. Ivey, Electrical and microstructural characterization of spinel phases as potential coatings for SOFC metallic interconnects, *J. Power Sources* 153 (2006) 114–124, <https://doi.org/10.1016/j.jpowsour.2005.03.137>.
- [26] C. Ostwald, H.J. Grabke, Initial oxidation and chromium diffusion. I. Effects of

- surface working on 9–20% Cr steels, *Corros. Sci.* 46 (2004) 1113–1127, <https://doi.org/10.1016/j.corsci.2003.09.004>.
- [27] S. Bagherifard, M. Guagliano, Fatigue behaviour of a low-alloy steel with nanostructured surface obtained by severe shot peening, *Eng. Fract. Mech.* 81 (2012) 56–68, <https://doi.org/10.1016/j.engfracmech.2011.06.011>.
- [28] S. Benafia, D. Reira, S.Y. Brou, B. Panicaud, J.L.G. Poussard, Influence of Surface Mechanical Attrition Treatment on the oxidation behaviour of 316L stainless steel, *Corros. Sci.* 136 (2018) 188–200, <https://doi.org/10.1016/j.corsci.2018.03.007>.
- [29] R.K.S. Raman, J.B. Gnanamoorthy, Influence of prior-austenite grain size on the oxidation behaviour of 9 wt.% Cr-1 wt.% Mo steel, *Oxid. Met.* 38 (1992) 483–496, <https://doi.org/10.1007/BF00665665>.
- [30] M. Shamsanaei, S. Pour-Ali, A.-R. Kiani-Rashid, S. Virtanen, Carbide fragmentation and dissolution in a high-carbon high-chromium steel using hot rolling process: microstructure evolution, wear, high temperature oxidation and chloride induced corrosion properties, *Corrosion* (2018), <https://doi.org/10.5006/2749>.
- [31] F. Abe, H. Araki, H. Yoshida, M. Okada, R. Watanabe, The effect of grain size on the corrosion behaviour of Inconel 600 in high-temperature steam, *Corros. Sci.* 21 (1981) 819–842, [https://doi.org/10.1016/0010-938X\(81\)90024-X](https://doi.org/10.1016/0010-938X(81)90024-X).
- [32] S. Pour-Ali, A.-R. Kiani-Rashid, A. Babakhani, S. Virtanen, M. Allieta, Correlation between the surface coverage of severe shot peening and surface microstructural evolutions in AISI 321: A TEM, FE-SEM and GI-XRD study, *Surf. Coat. Technol.* 334 (2018) 461–470, <https://doi.org/10.1016/j.surfcoat.2017.11.062>.
- [33] S. Pour-Ali, A.-R. Kiani-Rashid, A. Babakhani, S. Virtanen, Thermal stability of nanocrystalline surface layer of AISI 321 stainless steel, *Vacuum* 146 (2017) 297–303, <https://doi.org/10.1016/j.vacuum.2017.09.053>.
- [34] S. Pour-Ali, A.-R. Kiani-Rashid, A. Babakhani, Surface nanocrystallization and gradient microstructural evolutions in the surface layers of 321 stainless steel alloy treated via severe shot peening, *Vacuum* 144 (2017) 152–159, <https://doi.org/10.1016/j.vacuum.2017.07.016>.
- [35] S. Pour-Ali, A.-R. Kiani-Rashid, A. Babakhani, S. Virtanen, Severe shot peening of AISI 321 with 1000% and 1300% coverages: a comparative study on the surface nanocrystallization, phase transformation, sub-surface microcracks, and micro-hardness, *Int. J. Mater. Res.* 109 (2018) 451–459, <https://doi.org/10.3139/146.111622>.
- [36] J. Froitzheim, H. Ravash, E. Larsson, L.-G. Johansson, J.-E. Svensson, Investigation of chromium volatilization from FeCr interconnects by a denuder technique, *J. Electrochem. Soc.* 157 (2010) B1295–B1300, <https://doi.org/10.1149/1.3462987>.
- [37] L.A. Giannuzzi, F.A. Stevie, A review of focused ion beam milling techniques for TEM specimen preparation, *Micron* 30 (1999) 197–204, [https://doi.org/10.1016/S0968-4328\(99\)00005-0](https://doi.org/10.1016/S0968-4328(99)00005-0).
- [38] S. Pour-Ali, A. Kiani-Rashid, A. Babakhani, Improved corrosion inhibition of 3-amino-1, 2, 4-triazole on mild steel electrode in HCl solution using surface nanocrystallization, *Int. J. Mater. Res.* 107 (2016) 1031–1040, <https://doi.org/10.3139/146.111432>.
- [39] S. Pour-Ali, A. Kiani-Rashid, A. Babakhani, A. Davoodi, Enhanced protective properties of epoxy/polyaniline-camphorsulfonate nanocomposite coating on an ultrafine-grained metallic surface, *Appl. Surf. Sci.* 376 (2016) 121–132, <https://doi.org/10.1016/j.apsusc.2016.03.131>.
- [40] D. Raabe, Microstructure and crystallographic texture of strip-cast and hot-rolled austenitic stainless steel, *Metall. Mater. Trans. A* 26 (1995) 991–998, <https://doi.org/10.1007/BF02649096>.
- [41] D. Raabe, Texture and microstructure evolution during cold rolling of a strip cast and of a hot rolled austenitic stainless steel, *Acta Mater.* 45 (1997) 1137–1151, [https://doi.org/10.1016/S1359-6454\(96\)00222-4](https://doi.org/10.1016/S1359-6454(96)00222-4).
- [42] Z.B. Wang, N.R. Tao, W.P. Tong, J. Lu, K. Lu, Diffusion of chromium in nanocrystalline iron produced by means of surface mechanical attrition treatment, *Acta Mater.* 51 (2003) 4319–4329, [https://doi.org/10.1016/S1359-6454\(03\)00260-X](https://doi.org/10.1016/S1359-6454(03)00260-X).
- [43] S.J. Rothman, L.J. Nowicki, G.E. Murch, Self-diffusion in austenitic Fe-Cr-Ni alloys, *J. Phys. F Met. Phys.* 10 (1980) 383.
- [44] G.S. Was, S. Teyssyre, Z. Jiao, Corrosion of austenitic alloys in supercritical water, *Corros* 62 (2006) 989–1005, <https://doi.org/10.5006/1.3278237>.
- [45] E. Subbarao, *Solid Electrolytes and Their Applications*, Springer Science & Business Media, 2012.
- [46] Y. Li, S. Wang, P. Sun, D. Xu, M. Ren, Y. Guo, G. Lin, Early oxidation mechanism of austenitic stainless steel TP347H in supercritical water, *Corros. Sci.* 128 (2017) 241–252, <https://doi.org/10.1016/j.corsci.2017.09.023>.
- [47] X. Zhong, E.-H. Han, X. Wu, Corrosion behaviour of Alloy 690 in aerated supercritical water, *Corros. Sci.* 66 (2013) 369–379, <https://doi.org/10.1016/j.corsci.2012.10.001>.
- [48] G.C. Allen, P.M. Tucker, Multiplet splitting of X-ray photoelectron lines of chromium complexes. The effect of covalency on the 2p core level spin-orbit separation, *Inorganica Chim. Acta* 16 (1976) 41–45, [https://doi.org/10.1016/S0020-1693\(00\)91689-X](https://doi.org/10.1016/S0020-1693(00)91689-X).
- [49] G.C. Allen, S.J. Harris, J.A. Jutson, J.M. Dyke, A study of a number of mixed transition metal oxide spinels using X-ray photoelectron spectroscopy, *Appl. Surf. Sci.* 37 (1989) 111–134, [https://doi.org/10.1016/0169-4332\(89\)90977-X](https://doi.org/10.1016/0169-4332(89)90977-X).
- [50] Y. Behnamian, A. Mostafaei, A. Kohandehghan, B.S. Amirkhiz, D. Serate, Y. Sun, S. Liu, E. Aghaie, Y. Zeng, M. Chmielus, A comparative study of oxide scales grown on stainless steel and nickel-based superalloys in ultra-high temperature supercritical water at 800 °C, *Corros. Sci.* 106 (2016) 188–207, <https://doi.org/10.1016/j.corsci.2016.02.004>.
- [51] M.R. Ardigo-Besnard, I. Popa, O. Heintz, R. Chassagnon, M. Vilasi, F. Herbst, P. Girardon, S. Chevalier, Effect of surface finishing on the oxidation behaviour of a ferritic stainless steel, *Appl. Surf. Sci.* 412 (2017) 196–206, <https://doi.org/10.1016/j.apsusc.2017.03.280>.
- [52] X. Xu, X. Zhang, X. Sun, Z.P. Lu, Effects of silicon additions on the oxide scale formation of an alumina-forming austenitic alloy, *Corros. Sci.* 65 (2012) 317–321, <https://doi.org/10.1016/j.corsci.2012.08.039>.
- [53] S. Wang, Y. Hu, K. Fang, W. Zhang, X. Wang, Effect of surface machining on the corrosion behaviour of 316 austenitic stainless steel in simulated PWR water, *Corros. Sci.* 126 (2017) 104–120, <https://doi.org/10.1016/j.corsci.2017.06.019>.
- [54] J.-H. Kim, B.K. Kim, D.-I. Kim, P.-P. Choi, D. Raabe, K.-W. Yi, The role of grain boundaries in the initial oxidation behaviour of austenitic stainless steel containing alloyed Cu at 700 °C for advanced thermal power plant applications, *Corros. Sci.* 96 (2015) 52–66, <https://doi.org/10.1016/j.corsci.2015.03.014>.
- [55] R.E. Lobnig, H.P. Schmidt, K. Hennesen, H.J. Grabke, Diffusion of cations in chromia layers grown on iron-base alloys, *Oxid. Met.* 37 (1992) 81–93, <https://doi.org/10.1007/BF00665632>.
- [56] I. Saeki, H. Konno, R. Furuichi, T. Nakamura, K. Mabuchi, M. Itoh, The effect of the oxidation atmosphere on the initial oxidation of type 430 stainless steel at 1273 K, *Corros. Sci.* 40 (1998) 191–200, [https://doi.org/10.1016/S0010-938X\(97\)00113-3](https://doi.org/10.1016/S0010-938X(97)00113-3).
- [57] Y. Chen, Z. Liu, S.P. Ringer, Z. Tong, X. Cui, Y. Chen, Selective oxidation synthesis of MnCr<sub>2</sub>O<sub>4</sub> spinel nanowires from commercial stainless steel foil, *Cryst. Growth Des.* 7 (2007) 2279–2281, <https://doi.org/10.1021/cg070514a>.
- [58] R. Sachitanand, M. Sattari, J.-E. Svensson, J. Froitzheim, Evaluation of the oxidation and Cr evaporation properties of selected FeCr alloys used as SOFC interconnects, *Int. J. Hydrogen Energy* 38 (2013) 15328–15334, <https://doi.org/10.1016/j.ijhydene.2013.09.044>.
- [59] B. Hua, Y. Kong, W. Zhang, J. Pu, B. Chi, L. Jian, The effect of Mn on the oxidation behaviour and electrical conductivity of Fe–17Cr alloys in solid oxide fuel cell cathode atmosphere, *J. Power Sources* 196 (2011) 7627–7638, <https://doi.org/10.1016/j.jpowsour.2011.05.007>.